

Methylammonium Bromide Assisted Crystallization for Enhanced Lead-Free Double Perovskite Photovoltaic Performance

Hua Wu,* Yunfei Wang, Aijie Liu, Junxin Wang, Byeong Jo Kim, Yawen Liu, Yuan Fang, Xiaoliang Zhang,* Gerrit Boschloo, and Erik M. J. Johansson*

$\text{Cs}_2\text{AgBiBr}_6$ has recently gained wide attention as a possible alternative to lead-halide perovskites, considering the nontoxicity and improved stability. However, this double perovskite suffers from defects, especially deep electron traps, severely hampering the photovoltaic performance. This work reports a simple method to control the double perovskite crystallization by adding volatile salts into the precursor solution. X-ray diffraction patterns reveal that the organic cation with suitable radius (such as methylammonium, MA^+) is introduced into the perovskite lattice, forming an organic/inorganic mixed double perovskite intermediate phase. The organic salt is thereafter fully evaporated during high temperature annealing, and the all-inorganic double perovskite is obtained with dense surface and less pin-holes. From optical and electrical characterization, it is concluded that the $\text{Cs}_2\text{AgBiBr}_6$ film exhibits high quality, with higher light absorptance and emission. Reduced trap density and longer carrier lifetime are also observed. The improved $\text{Cs}_2\text{AgBiBr}_6$ film is beneficial for efficient carrier collection with suppressed defect-assisted recombination. With this strategy, a power conversion efficiency (PCE) of 2.53% is achieved for the champion $\text{Cs}_2\text{AgBiBr}_6$ -based solar cell device, which is significantly higher compared to the control device with 1.43% PCE. This work is therefore helpful for further improvement of inorganic lead-free perovskite materials for optoelectronic applications.

25.6%.^[2] The impressive photovoltaic performances have also extended the applications of perovskites to other fields, such as light emitting devices^[3] and photo-detectors.^[4] Their excellent performance are benefitting from the high absorption coefficient, long carrier diffusion length, high carrier mobilities, and the unique defect tolerance.^[5] Nevertheless, their toxic nature caused by the presence of lead (Pb) in the chemical compositions and the structural instability have been considered as two major issues for commercialization.^[6] Hence, it becomes necessary to find suitable alternatives for more environmental-friendly metal halide materials.^[7]

Recently, bismuth (Bi) based materials have shown great promise for Pb-replacement, due to their low toxicity and Bi^{3+} being isoelectronic with Pb^{2+} .^[8] The Bi-based double perovskites, $\text{Cs}_2\text{AgBiX}_6$ ($\text{X} = \text{Br}, \text{Cl}$) have been fabricated and investigated experimentally and theoretically, attracting great attention in recent few years.^[9] This type double perovskite

exhibit elpasolite structure, formed by corner-sharing octahedra, with alternating Ag or Bi in the center of octahedra. They can absorb visible light and have excellent ambient stability. In addition to the stable light-absorber property, $\text{Cs}_2\text{AgBiBr}_6$ was reported to have a long photocarrier lifetime

1. Introduction

Lead-halide perovskite solar cells have attracted wide attention since the first demonstration in 2009,^[1] with rapidly rising power conversion efficiency (PCE) from 3% to new record of

H. Wu, A. Liu, B. J. Kim, Y. Liu, G. Boschloo, E. M. J. Johansson
Department of Chemistry-Ångström
Physical Chemistry
Uppsala University
Uppsala 75120, Sweden
E-mail: huawu9107@gmail.com; erik.johansson@kemi.uu.se

Y. Wang, X. Zhang
School of Materials Science and Engineering
Beihang University
Beijing 100191, China
E-mail: xiaoliang.zhang@buaa.edu.cn

J. Wang
Chemistry Research Laboratory
Department of Chemistry
University of Oxford
12 Mansfield Road, Oxford OX1 3TA, UK

Y. Fang
Department of Applied Physical Chemistry
KTH Royal Institute of Technology
Stockholm 114 28, Sweden

 The ORCID identification number(s) for the author(s) of this article can be found under <https://doi.org/10.1002/adfm.202109402>.

© 2021 The Authors. Advanced Functional Materials published by Wiley-VCH GmbH. This is an open access article under the terms of the Creative Commons Attribution-NonCommercial-NoDerivs License, which permits use and distribution in any medium, provided the original work is properly cited, the use is non-commercial and no modifications or adaptations are made.

DOI: 10.1002/adfm.202109402

reaching 1.4 μs , and high photo-excited carrier density of $2.2 \times 10^{16} \text{ cm}^{-3}$ under 1 sun, an order of magnitude higher than lead-iodide perovskites.^[10] Moreover, double perovskites show relatively low charge carrier effective mass, which favors the charge transport and extraction process, close to those of lead-iodide perovskites.^[11] Also, $\text{Cs}_2\text{AgBiBr}_6$ needs a large activation energy for ion movement, preventing the vacancy defect formation during halide migration under external bias.^[12] Therefore, these superior optical and electrical properties render Bi-based double perovskites as promising candidates for low-toxic and stable photovoltaic applications.

Great efforts have been taken on $\text{Cs}_2\text{AgBiBr}_6$ solar cells, through material quality and device structure engineering. Some fabrication methods, such as low-pressure assisted crystallization,^[13] antisolvent treatment,^[14] annealing process adjustment^[15] have been developed, with a result of improved $\text{Cs}_2\text{AgBiBr}_6$ film morphology and PCEs. Compositional engineering, such as cation doping^[16] and anion modification by sulfide,^[17] was adopted to improve the light harvesting ability of $\text{Cs}_2\text{AgBiBr}_6$ double perovskites, leading to higher photocurrent as well as higher PCE. Also engineering charge extraction and charge transport with different hole transport materials (HTMs)^[18] and electron transport materials (ETM),^[19] has been an efficient route to enhance PCE. Furthermore, in a few reports interfacial layers were introduced between ETM/perovskite or HTM/perovskite,^[20] not only passivating the interfacial defects but also extend photo-absorption. Interfacial engineering is proved to be an efficient method to improve PCE, especially, boosting the PCE of $\text{Cs}_2\text{AgBiBr}_6$ solar cell to more than 3%.

The charge carrier diffusion length and carrier mobility has previously been investigated, suggesting that a short electron diffusion length ($\approx 30 \text{ nm}$) and a high density of electron traps mainly limit the photovoltaic performance for $\text{Cs}_2\text{AgBiBr}_6$ solar cells.^[11b] Several theoretical studies suggested abundant trap sites were easily formed in $\text{Cs}_2\text{AgBiBr}_6$ double perovskites. Hence, elimination of bulk trap sites within the $\text{Cs}_2\text{AgBiBr}_6$ film can benefit the PCE of solar cells. According to a previous report, the methylammonium (MA^+) cation can form higher crystallinity perovskites and heal the deep trap sites due to its large radius and dipolar nature.^[21] MA-halide salts have also been introduced to assist all-inorganic cesium lead halide perovskites formation with ordered structure and enhanced solar cell performance.^[22] However, reports about regulation of the crystallization process through additives to suppress defect formation is lacking for $\text{Cs}_2\text{AgBiBr}_6$ double perovskites.

In this work, we report a Cs/MA cation-mixed intermediate phase strategy by adding volatile MABr salt into the $\text{Cs}_2\text{AgBiBr}_6$ precursor solution, leading to high-quality double perovskite formation. During high-temperature annealing, MA^+ was evaporated and replaced by Cs^+ , resulting in full conversion to all-inorganic double perovskite. With this strategy, the optimized double perovskite films exhibited improved optical absorption and emission, as well as improved surface morphology observed in scanning electron microscopy (SEM) images. Reduced trap site density and extended carrier lifetime are obtained for the optimized double perovskite films, compared to the control sample. Electron extraction from perovskite to the ETM tended to be more efficient and defect-assisted recombination was suppressed efficiently, which was attributed to the reduced number of trap sites. As a result, the solar cells

fabricated from optimized films yielded a champion PCE of 2.53%, much higher than the control sample PCE of 1.43%.

2. Results and Discussion

2.1. Cation Exchange Process

The photoactive layer $\text{Cs}_2\text{AgBiBr}_6$ was deposited via a one-step method by spin-coating the precursor solution. A volatile organic salt, methylammonium bromide (MABr), is added into $\text{Cs}_2\text{AgBiBr}_6$ precursor solution. Different contents of MABr adding into precursor solution were investigated. For simplicity, the samples are denoted as $\text{Cs}_2\text{AgBiBr}_6\text{-}x\text{MABr}$, where x represents the molar ratio of $\text{Cs}_2\text{AgBiBr}_6$ to MABr (1: x of $\text{Cs}_2\text{AgBiBr}_6$: MABr) in the precursor solution. It should be noted that the final double perovskite films after annealing do not contain MA (shown below). As shown in Figure S1a, Supporting Information, the main characteristic peaks of XRD patterns for all samples are almost identical to the control $\text{Cs}_2\text{AgBiBr}_6$ film, indexing to (110), (200), (202), (311), (222), (400), (313), (402), (422), (511), (404) for double perovskite phase. Detailed fabrication information can be found in the experimental section.

Optical absorption for these samples were measured and are shown in Figure S2, Supporting Information, together with bandgap energy calculations from Tauc plots. An increase in absorptance in the wavelength region lower than 500 nm was observed for samples formed with MABr (Figure S2b, Supporting Information). By comparing their corresponding transmittance and reflectance spectra (in Figure S2a, Supporting Information), the change of absorptance mainly arise from the decreased reflectance, while the transmittance for all samples were almost the same. Since optical reflectance is highly dependent on film morphology, SEM measurement was conducted for surface analysis (Figure S2e–h, Supporting Information), indicating an optimized ratio of 1.0MABr. As illustrated in Figure 1b,c, the $\text{Cs}_2\text{AgBiBr}_6\text{-}1.0\text{MABr}$ sample presents a better film morphology, with denser grains and less pin-holes compared to the control sample. Besides, the SEM images exhibit an increase of the average crystal grain size from 420 to 640 nm with the adding of MABr in the precursor solution.

We performed the X-ray photoelectron spectroscopy (XPS) to investigate the existence of MABr in the $\text{Cs}_2\text{AgBiBr}_6\text{-}1.0\text{MABr}$ before annealing, the N 1s spectra shown in Figure 1d. An obvious N 1s peak was observed in the sample of $\text{Cs}_2\text{AgBiBr}_6\text{-}1.0\text{MABr}_i$ (initially spin-coated film without annealing), demonstrating the existence of MA^+ cation at this stage. After annealing (280°), MABr was fully removed, evidenced by the disappeared N 1s signal, obtaining an all-inorganic film.

In order to understand the role of MABr during double perovskite formation process, we performed X-ray diffraction (XRD) measurements of initially spin-coated $\text{Cs}_2\text{AgBiBr}_6$ and $\text{Cs}_2\text{AgBiBr}_6\text{-}1.0\text{MABr}$ films. In Figure S1b, Supporting Information, and Figure 1e, XRD spectra exhibited characteristic peaks $\approx 2\theta = 15^\circ$ and 31° , ascribed to (200) and (400) plane, respectively. XRD peaks of $\text{Cs}_2\text{AgBiBr}_6\text{-}1.0\text{MABr}_i$ shift to smaller angle compared to $\text{Cs}_2\text{AgBiBr}_6$ film, which agree with MA^+ cations incorporating into the crystal lattice.

In order to understand the effect of MA^+ on the crystal lattice of double perovskite, we also carried out the first-principle

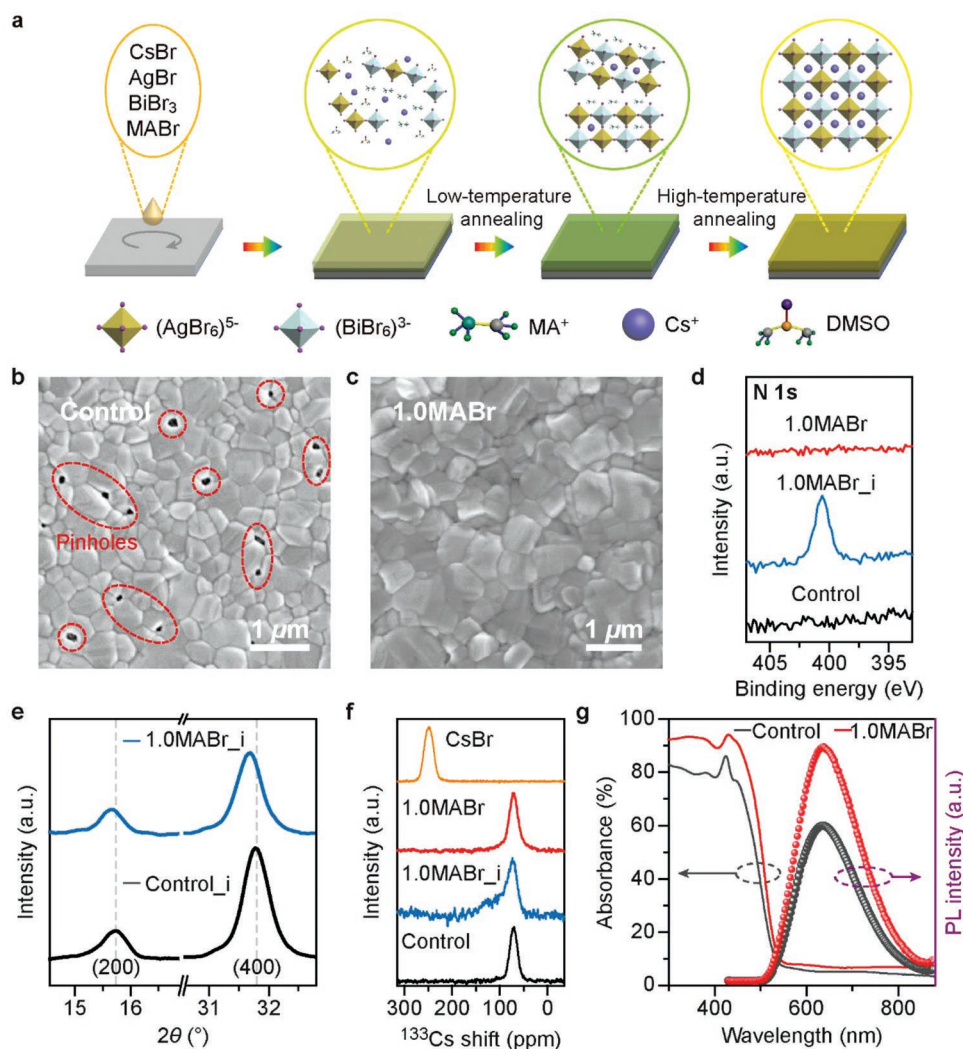


Figure 1. a) The schematic illustration of MABr additive assisted double perovskite crystallization process, where at low temperature Cs/MA mixed-cation intermediate phase was formed, then MA evaporated at high temperature, obtaining all-inorganic double perovskite phase. Top-view surface morphology of b) control $\text{Cs}_2\text{AgBiBr}_6$ and c) $\text{Cs}_2\text{AgBiBr}_6$ -1.0MABr films. Scale bar: 1 μm . d) N 1s XPS measurements of the materials: 1.0MABr_i represents the $\text{Cs}_2\text{AgBiBr}_6$ -1.0MABr_i film without annealing. e) XRD patterns for control $\text{Cs}_2\text{AgBiBr}_6$ and $\text{Cs}_2\text{AgBiBr}_6$ -1.0MABr films at initial stage. f) Static NMR measurements of the materials, ^{133}Cs spectra detected: 1.0MABr_i represents the $\text{Cs}_2\text{AgBiBr}_6$ -1.0MABr_i film without annealing. g) Optical absorption and photoluminescence spectra of the control double perovskite film and 1.0MABr-assisted double perovskite film.

calculations based on the density functional theory (DFT) to study the mixed-cation (CsMA) double perovskite systems. To model the CsMA double perovskites, we substituted Cs^+ cations with MA^+ in the bulk model. Detailed information can be found in computational method in supporting information. In Figure S3, Supporting Information, we illustrate the double perovskite structure with MA:Cs ratio ranging from 1:0 to 0:1. The DFT results indicate that large amount of MA (when Cs: MA less than 1:1) will induce serious lattice distortion, deviating from the cubic perovskite structure, especially the sample of MA_8Cs_0 , which agrees with previous report of $\text{MA}_2\text{AgBiBr}_6$.^[23] With less MA^+ doping, the double perovskite keeps stable cubic lattice, but exhibiting larger lattice constant, induced from the larger radius of MA^+ than Cs^+ .

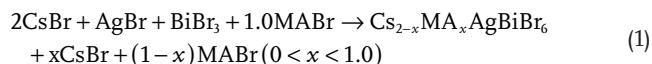
Therefore, we suggest that the XRD peak shift for the $\text{Cs}_2\text{AgBiBr}_6$ -1.0MABr_i sample is ascribed to the lattice expansion from larger MA^+ ion incorporation. The shift of peak position

remained after annealing both the control sample and the $\text{Cs}_2\text{AgBiBr}_6$ -1.0MABr sample at low temperature of 100 °C (Figure S1b, Supporting Information). According to Figure S1c, Supporting Information, the characteristic peaks are at same position for both samples after 280 °C annealing, demonstrating the removal of MA and formation of pure $\text{Cs}_2\text{AgBiBr}_6$ phase.^[22b]

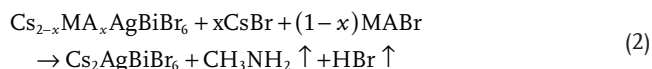
Static nuclear magnetic resonance (NMR) measurements, as a sensitive tool for composition analysis, were also carried out. The control $\text{Cs}_2\text{AgBiBr}_6$ double perovskite exhibits a relatively narrow peak at 70.2 ppm. We then look at the measurement of $\text{Cs}_2\text{AgBiBr}_6$ -1.0MABr_i, corresponding to the sample we studied in XRD and XPS. The peak broadens, and an extra peak emerged at 120 ppm. According to previous report,^[22b] the broadening can be due to the presence of cesium sites with different numbers of nearest neighbor MA^+ in the neighboring cubo-octahedral cages,^[22b] and the presence of CsBr can be excluded. We suggest the two broad peaks correspond to the

disordered mixed-cation MA/Cs double perovskite phase. The annealed Cs₂AgBiBr₆-1.0MABr yields only one narrow peak at 70.2 ppm, exactly the same as the control sample, indicating the fully transformation to all-inorganic double perovskite phase.

We therefore suggest the MABr-assisted crystallization process described in Figure 1a. At the initial stage, the organic cation MA⁺ can be included in the double perovskite lattice, which leads to the formation of an intermediate phase Cs_{2-x}MA_xAgBiBr₆ (0 < x < 1.0), along with free CsBr and MABr. The process is expressed as:



With the volatilization of MABr during thermal annealing, free Cs⁺ replaces the MA⁺, and the intermediate phase transforms to the inorganic Cs₂AgBiBr₆ phase. As the MABr is decomposed to MA gas and hydro bromide acid gas under annealing,^[24] this process can be expressed as:



As reported by previous report,^[25] excess volatile salt additive in precursor allows for better crystal growth, leading to better film morphology by changing the activation energy for the perovskite crystallization. Thus, MABr, as an effective volatile additive in precursor, can slow down the crystallization process for Cs₂AgBiBr₆ double perovskites, dominated by the additive removal process going from a mixed MA/Cs phase to the Cs₂AgBiBr₆ double perovskite phase, leading to larger grain sizes. Moreover, considering to the strong interaction between MA⁺ and TiO₂ compared to the inorganic phase and TiO₂, (indicated by the Ti 2p XPS peak shift in Figure S1e, Supporting Information)^[22b] this MA/Cs mixed double perovskite intermediate phase may induce better crystallization, resulting in higher quality double perovskite film. As shown in Figure 1g, an increased emission intensity is also observed for the Cs₂AgBiBr₆-1.0MABr sample.

2.2. Energy Level Mapping and Defect Property Analysis

In addition to film quality, energy level alignment is another critical factor for achieving efficient solar cells. In order to determine the energy levels of double perovskites, we performed Kelvin probe measurements for work function estimation and XPS measurements for valence band determination. We deposited Cs₂AgBiBr₆ and Cs₂AgBiBr₆-1.0MABr films on meso-TiO₂ for the measurements. Considering the surface-sensitive nature, we performed a surface scan of 650 μm × 650 μm on both samples (see Figure S4, Supporting Information) in dark condition. The average of work function values are 5.23 and 4.72 eV for Cs₂AgBiBr₆ and Cs₂AgBiBr₆-1.0MABr, respectively. The shift of Fermi level is related to defect density within the semiconductors.

XPS measurement can be used to study the valence band maximum (VBM) of perovskites. Using the same procedure as in our previous study,^[26] we performed valence band spectra on both control sample and 1.0MABr film deposited on meso-TiO₂

substrate. Proper calibration in binding energy scale is essential to obtain accurate information from XPS. The obtained XPS spectra in this work were all calibrated with an Gold (Au) coated sample. Specifically, a thin Au was deposited on a part of the surface of the double perovskite film. The obtained spectra then were energy calibrated based on the binding energy of Au 4f_{7/2} peak position. The VBM values can be determined using semi-log extrapolation method, as shown in Figure S5a, Supporting Information, which has been reported to be more accurate than linear extrapolation method.^[27] The control sample and 1.0MABr film show obviously different VBMs, 0.6 and 1.3 eV, respectively, where Fermi level energy is set to 0 eV. Combining with the results of bandgap energy, we can determine the energy level structures, as the diagram in Figure S5b, Supporting Information.

Obviously, the MABr-assisted double perovskite showed a near intrinsic semiconductor behavior, while the control sample showed deep *p*-type doping. The shift of Fermi level suggests a big change of defect distribution. We quantitatively analyzed the trap density *n*_{trap} using a space-charge-limited currents (SCLC) method. Both electron-only devices and hole-only devices were fabricated to compare the trap density change after MABr optimization. As shown in Figure 2a–d, these current (*J*)–voltage (*V*) curves behaved in three different regimes: Ohmic (*J* ∝ *V*^{*n*} when *n* = 1), trap-filled (*J* ∝ *V*^{*n*} when *n* > 3) and Child's (*J* ∝ *V*^{*n*} when *n* = 2). The trap density *n*_{trap} can be estimated from the intersection point from Ohmic to trap-filled regime, called as trap-filled limit voltage (*V*_{TFL}). Their relationship is expressed as:^[12]

$$V_{TFL} = \frac{en_{trap}L^2}{2\epsilon\epsilon_0} \quad (3)$$

where ϵ_0 is vacuum permittivity, ϵ represents the relative dielectric constant, which is 51 for Cs₂AgBiBr₆,^[12] *e* and *L* mean elementary charge and film thickness, respectively. The calculated electron trap density for control Cs₂AgBiBr₆ film and 1.0MABr film are 5.3 × 10¹⁴ and 3.1 × 10¹⁴ cm⁻³, respectively. The calculated hole trap density for control Cs₂AgBiBr₆ film and 1.0MABr film are 2.2 × 10¹⁵ and 1.4 × 10¹⁵ cm⁻³, respectively. The lower trap density is consistent with our Fermi level analysis and PL study. In the Child's law regime, carrier mobility μ can be estimated by fitting *J*–*V* curves with Mott–Gurney law:^[12]

$$J_D = \frac{9}{8} \epsilon\epsilon_0 \mu \frac{V^2}{L^3} \quad (4)$$

The calculated electron mobility for control Cs₂AgBiBr₆ film and 1.0MABr film are 2.6 × 10⁻⁴ and 4.0 × 10⁻⁴ cm² V⁻¹ S⁻¹, respectively. The calculated hole mobility for control Cs₂AgBiBr₆ film and 1.0MABr film are 8.7 × 10⁻⁵ and 1.3 × 10⁻⁴ cm² V⁻¹ S⁻¹, respectively. The calculated trap density is quite comparable to that of lead-halide perovskites,^[28] suggesting the potential of this Cs₂AgBiBr₆ double perovskites in optoelectronic applications. An increased carrier mobility was also observed after MABr optimization. Therefore, the MABr modified double perovskite samples can be beneficial for photovoltaic applications, since lower trap density and higher carrier mobility are suggested from XPS and SCLC results.

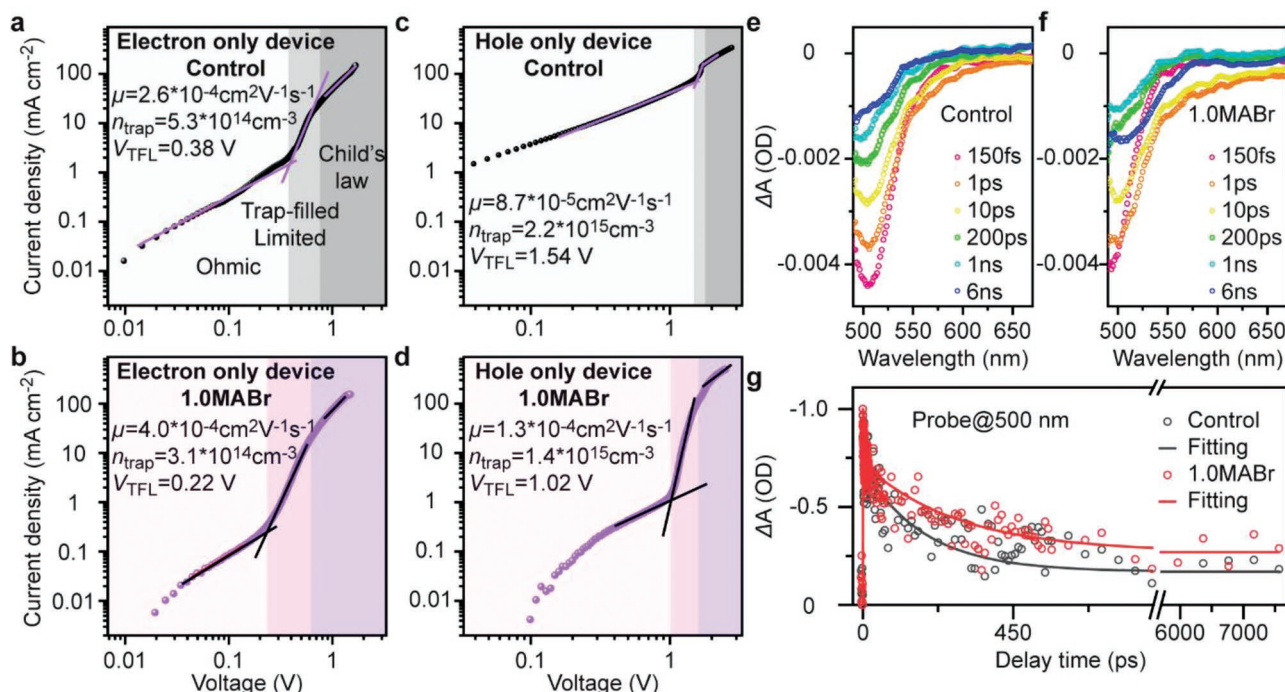


Figure 2. Dark J - V curves of electron-only devices employing a) control $\text{Cs}_2\text{AgBiBr}_6$ and b) $\text{Cs}_2\text{AgBiBr}_6$ -1.0MABr films, with device structure: FTO/ c - TiO_2 /meso- TiO_2 / $\text{Cs}_2\text{AgBiBr}_6$ /PCBM/Ag. Dark J - V curves of hole-only devices employing c) control $\text{Cs}_2\text{AgBiBr}_6$ and d) $\text{Cs}_2\text{AgBiBr}_6$ -1.0MABr films, with device structure: FTO/ NiO_x / $\text{Cs}_2\text{AgBiBr}_6$ /PTB7/Au. TAS at different time range following 400 nm laser excitation of e) control $\text{Cs}_2\text{AgBiBr}_6$ and f) $\text{Cs}_2\text{AgBiBr}_6$ -1.0MABr film deposited on pure glass. g) Normalized kinetic and fitting of the GSB when probing at 500 nm for control $\text{Cs}_2\text{AgBiBr}_6$ and $\text{Cs}_2\text{AgBiBr}_6$ -1.0MABr film.

2.3. Carrier Dynamic for Double Perovskite Film

Given the indirect bandgap, $\text{Cs}_2\text{AgBiX}_6$ double perovskites exhibit low photoluminescence quantum yield. Time-resolved photoluminescence (TRPL) measurements therefore could only characterize the decay of a small fraction of the photo-generated carriers.

In order to understand the decay kinetics thoroughly, we performed transient absorption spectroscopy (TAS) on the control film and the 1.0MABr film deposited on glass substrates. Figure 2e,f presents the TAS at different times after 400 nm laser pulse excitation, for the control film and the 1.0MABr film, respectively. A strong ground state bleaching (GSB) was observed for both samples centering ≈ 505 nm. The bleaching signal is related to the population of electrons in the excited states after pump and therefore reduced number of electrons in the ground state. Both control and 1.0MABr exhibits bleaching in the range of wavelength ≤ 570 nm, consistent with their similar bandgap energy. The bleach signal decayed over a few nanoseconds, dominated by charge recombination and charge carrier trapping. Previous studies have analyzed the bleach recovery kinetics to determine the charge carrier lifetime.^[19] Figure 2g compares the time-dependent bleach recovery traces for control film and 1.0MABr film, at 500 nm (around the bleach peak position). The solid lines in Figure 2g represent the results fitted by a widely used biexponential kinetic fit, where the fast decay process represents bimolecular recombination and the slow decay process is mainly ascribed to defect-assisted recombination.^[29] The fitting results are summarized in Table S2, Supporting Information. The average lifetime increases from

111 (control) to 171 ps (1.0MABr). The 1.0MABr sample exhibited large portion of long-lived carriers compared to control sample after 6 ns. The longer lifetime for the 1.0MABr film indicates reduced trap density after MABr-assisted growth.

2.4. Solar Cell Performance

To study the effect of MABr additive strategy in devices, photovoltaic performance was investigated for solar cells with the configuration of FTO/ c - TiO_2 /meso- TiO_2 / $\text{Cs}_2\text{AgBiBr}_6$ /poly[4,8-bis[(2-ethylhexyl)oxy]benzo[1,2- b :4,5- b']dithiophene-2,6-diyl-alt-3-fluoro-2-[(2-ethylhexyl)carbonyl]thieno[3,4- b]thiophene-4,6-diyl] (PTB7)/Au, as shown in Figure 3a,b. In this work, we employed PTB7 as hole transport layer, as it performed better than other common HTMs in this device structure (Figure S6, Supporting Information). Figure 3c compares the current density (J)-voltage (V) curves of $\text{Cs}_2\text{AgBiBr}_6$ prepared with different MABr ratio. Significant improvement can be observed with MABr incorporation, with $\text{Cs}_2\text{AgBiBr}_6$ -1.0MABr as the champion MABr concentration. Their corresponding photovoltaic parameters are summarized in Table 1. The PCE increased from 1.43% for the best control device to 2.53% for the champion 1.0MABr device, mainly benefitting from the enhancement in short-circuit J_{sc} (from 2.35 mA cm^{-2} for the control device to 3.50 mA cm^{-2} for the 1.0MABr device) and fill factor (FF) (from 0.66 for the control device to 0.76 for the 1.0MABr device). The increased J_{sc} and FF agrees well with the smaller series resistance and larger shunt resistance with MABr additive, compared to control sample in Table 1. Figure 3d shows the J - V curves of reverse scan and

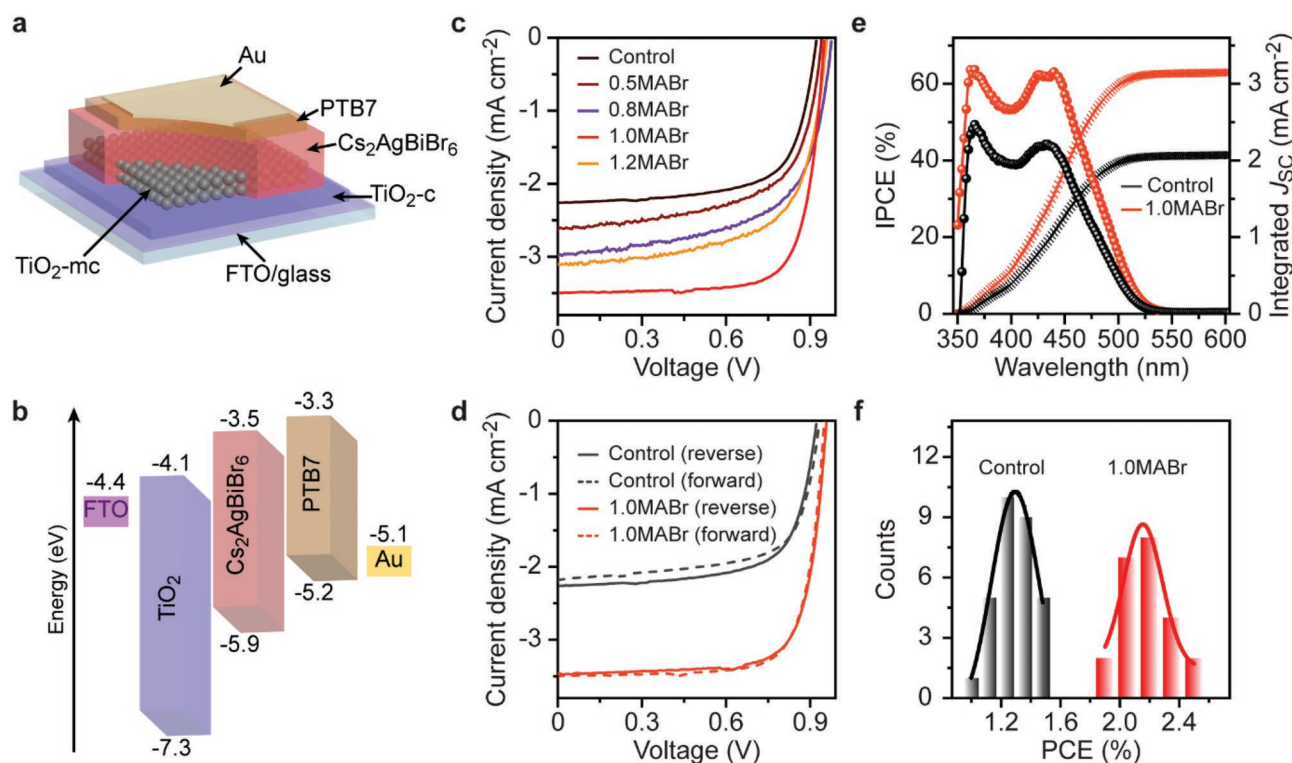


Figure 3. Solar cell performances. a) Schematic of architecture and b) energy level diagram for solar cell with FTO/c-TiO₂/meso-TiO₂/Cs₂AgBiBr₆/PTB7/Au. c) *J*-*V* curves of solar cells under AM1.5G with different amounts of MABr adding into precursor solution. d) *J*-*V* curves under both forward (dash line) and reverse (solid line) scan directions, for the champion device of control sample and 1.0MABr sample. e) Comparison of IPCE and integrated current density for solar cells made from control Cs₂AgBiBr₆ and Cs₂AgBiBr₆-1.0MABr. f) PCE distributions of control Cs₂AgBiBr₆ and Cs₂AgBiBr₆-1.0MABr solar cell devices (30 devices).

forward scan for the best control device and 1.0MABr device. Corresponding photovoltaic parameters are summarized in Table 2, both devices show negligible hysteresis. The good stability under different scan direction is probably related to the high activation energy for ion movement. The statistical diagram of photovoltaic parameters (*J*_{sc}, open-circuit voltage (*V*_{oc}), FF and PCE) of the cells with different amount of MABr additive is given in Figure S8, Supporting Information. For confirmation of the increased *J*_{sc} result, and for investigation of the photocurrent spectra, we conducted incident-photon-to-electron conversion efficiency (IPCE) measurement, and the results are shown in Figure 3e. The IPCE exhibited an onset wavelength of ≈540 nm, matching with the absorption spectra. Higher IPCE over the whole photo conversion range is achieved for the 1.0MABr device, therefore leading to higher photocurrent than the control

device. The integrated *J*_{sc} for the control device and the 1.0MABr device are 2.15 and 3.20 mA cm⁻², respectively. The smaller integrated current from IPCE than *J*-*V* scans is due to the discrepancy in illumination area during different measurement and the wavelength limitation of IPCE instrument measurement. Figure 3f shows the good reproducibility of PCE for the control device and the 1.0MABr device. The PCE for the 1.0MABr device ranges from 2 to 2.5%, clearly higher than the control devices.

2.5. Device Charge Carrier Kinetics

In order to get insights into the origin of the enhanced photovoltaic performance, light intensity-dependent measurements of *J*_{sc} and *V*_{oc} were conducted and are shown in Figure 4a,b.

Table 1. Summary of the photovoltaic parameters for solar cells with various photoactive layers.

PSCs	<i>V</i> _{oc} [V]	<i>J</i> _{sc} [mA cm ⁻²]	FF	PCE (Max.) [%]	PCE (Ave.) [%]	<i>R</i> _s [Ω cm ²]	<i>R</i> _{sh} [Ω cm ²]
Control	0.92	2.35	0.66	1.43	1.25	31	2307
0.5MABr	0.94	2.64	0.68	1.71	1.42	30	24569
0.8MABr	0.93	2.82	0.76	2.01	1.71	24	10014
1.0MABr	0.95	3.50	0.76	2.53	2.16	17	17565
1.2MABr	0.91	3.3	0.72	2.13	1.93	17	6708

Note: *R*_s represents the series resistance, and *R*_{sh} represents the shunt resistance of the device.

Table 2. Comparison of the photovoltaic performance for champion control device and 1.0MABr device.

PSCs	V_{oc} [V]	J_{sc} [mA cm^{-2}]	FF	PCE [%]
Control reverse	0.92	2.35	0.66	1.43
Control forward	0.93	2.28	0.65	1.38
1.0MABr reverse	0.95	3.50	0.76	2.53
1.0MABr forward	0.96	3.47	0.75	2.49

Note: reverse means the scanning direction is from open-circuit voltage to short circuit, and forward means the scanning direction is from short circuit to open-circuit voltage.

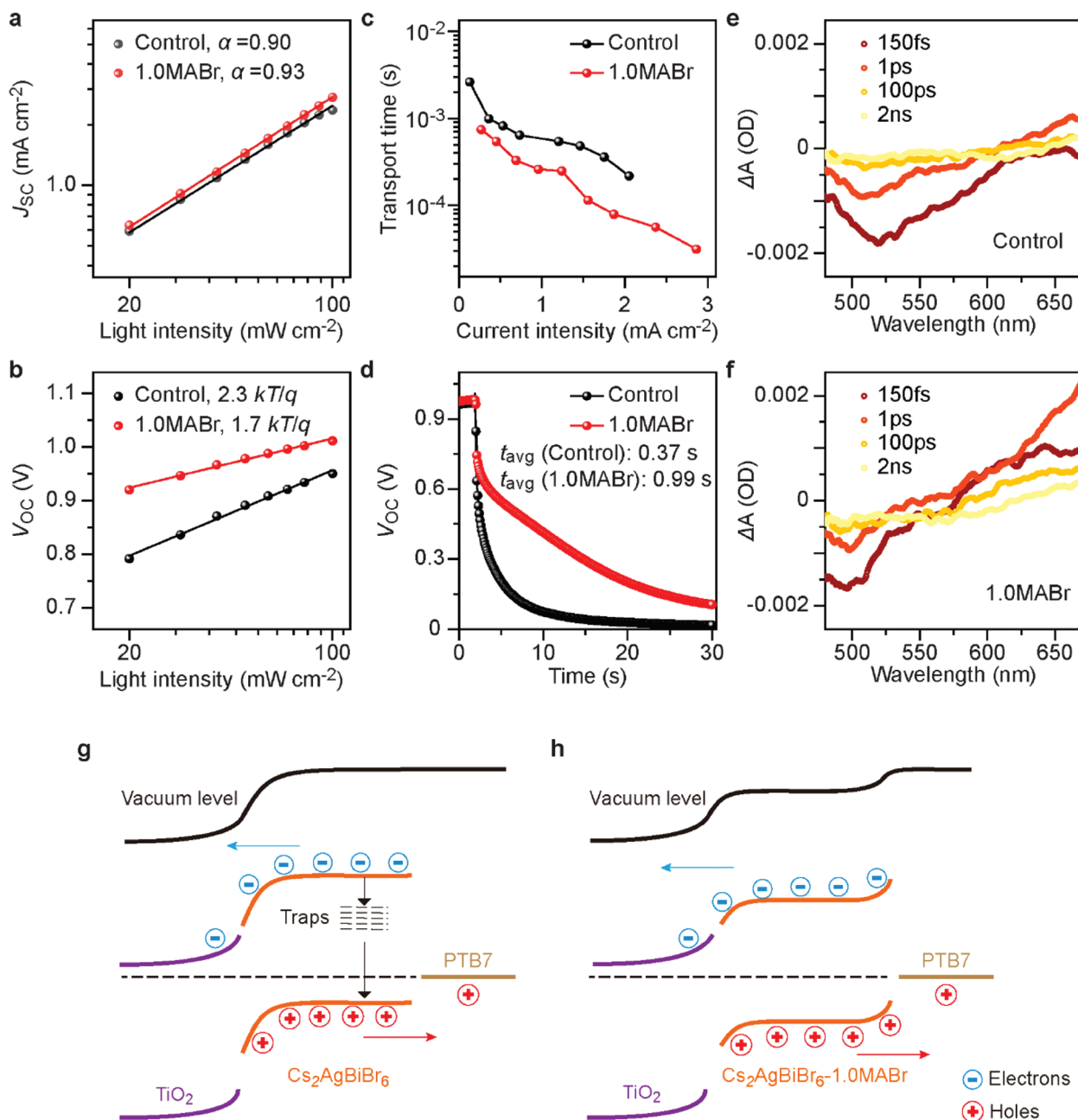


Figure 4. Charge carrier dynamics. Light intensity-dependent a) photocurrent and b) photo-voltage for control Cs₂AgBiBr₆ and Cs₂AgBiBr₆-1.0MABr solar cell devices. c) Comparison of the carrier transport lifetime within double perovskite solar cell devices as a function of light intensity. d) TPV decay for control Cs₂AgBiBr₆ and Cs₂AgBiBr₆-1.0MABr solar cells at open circuit condition. The time-resolved TAS following 400 nm laser excitation for e) control Cs₂AgBiBr₆ and f) Cs₂AgBiBr₆-1.0MABr, deposited on TiO₂ substrates. The schematic illustration of charge carrier transport/recombination and energy band structure within the g) control Cs₂AgBiBr₆ and h) Cs₂AgBiBr₆-1.0MABr based solar cells.

With increasing light intensity, J_{SC} increases sub-linearly, following: $J_{SC} \propto I^\alpha$.^[30] The value of fitting coefficient α increases from 0.90 for control device to 0.93 for 1.0MABr device. The value of α for both devices are close to unity, meaning that bimolecular recombination can be negligible during carrier extraction at short-circuit condition. Figure 4b shows the relationship between V_{OC} and light intensity. Based on previous report, V_{OC} is linearly dependent on the natural logarithm of light intensity, with a slope of $\frac{nkT}{q}$, where n , k , T , q are ideality factor, Boltzmann constant, temperature (in Kelvin) and elementary charge, respectively.^[30] Generally, value of n close to 1 indicates that trap-assisted recombination is low in device and bimolecular recombination is dominant at open circuit condition. The control device presents a strong dependence with light intensity, as n of 2.3, while the 1.0MABr device shows a smaller n of 1.7. The lower n value for 1.0MABr device suggests a reduced trap-assisted recombination, agreeing well with our SCLC results, thus leading to an improved photovoltaic performance.

We further studied the carrier dynamic within devices by transient photocurrent (TPC) and transient photovoltage (TPV). In Figure 4c, the charge carrier transport times were extracted from TPC measurements, by introducing a small modulation of the light illumination with various intensity at short circuit condition. The 1.0MABr-based device showed a shorter transport time, evidencing a more efficient charge carrier transport compared to control device, explaining the increased J_{SC} . The faster charge carrier transport for 1.0MABr sample can be attributed to the decreased trap density for the $Cs_2AgBiBr_6$ -1.0MABr film. Figure 4d shows the TPV of solar cells with control and 1.0MABr double perovskites, respectively. As expected, the 1.0MABr-based solar cell shows relatively longer charge carrier lifetime, which suggests that the 1.0MABr based device exhibits a slower charge recombination, and a slower ion transport within the cell due to less ion vacancies. The slower recombination may stem from the reduced trap-related recombination, which is advantageous in solar cells and can explain the enhanced V_{OC} and FF. The slow ion movement agrees with low hysteresis observed in Figure 3d. We also performed TPV with a smaller light modulation on a faster time scale, and the results are shown in Figure S9, Supporting Information. The results show that there are also recombination processes on a short timescale, which are still present in the 1.0MABr-based solar cell.

To gain further insight on how the trap sites affect the charge extraction behaviors, we studied the transfer properties of the photogenerated charge carriers. Steady-state PL quenching for the control sample and 1.0MABr film were performed, as shown in Figure S10, Supporting Information. When coating PTB7 (HTM) on top, a serious PL quenching was observed for both control sample and 1.0MABr, indicating an efficient hole transfer in our devices. The appeared PL peak is ascribed to PTB7 emission. Figure S10b, Supporting Information, records their TRPL after excited by 405 nm laser. The fast decay for PTB7 coated samples indicates an efficient hole transfer from double perovskite to PTB7.

It is difficult to analyze electron transfer process through PL measurements, since the meso-TiO₂ has huge effect on crystallinity and therefore on PL intensity (Figure S11, Supporting Information). We therefore performed TAS measurements on the control film and 1.0MABr film deposited on meso-TiO₂

substrate to study the electron transfer process. The time-resolved TAS for both samples are presented in Figure 4e,f. Except for the GSB, an induced absorption bands from 600 nm appeared, which according to other reports is attributed to the absorption of transient species induced from electron collection in TiO₂.^[31] The 1.0MABr sample shows much stronger positive signal, as compared to control sample, suggesting a more efficient electron transfer from 1.0MABr-assisted double perovskite to TiO₂ ETM. Therefore, it can be concluded that the MABr-assisted double perovskite exhibited suppressed defect formation, promoting more efficient electron transfer contributing to higher photocurrent.

The enhanced electron collection can also be observed from light illumination induced surface photovoltage (SPV), through Kelvin probe measurement. Specifically, Kelvin probe measures the difference of the contact potential difference (CPD) between Kelvin probe tip and sample. The SPV can be estimated via $SPV = CPD_{light} - CPD_{dark}$. In Figure S12, Supporting Information, the CPD under dark condition are set to 0 eV for easy comparison. Under light illumination, the SPV values become negative (≈ -0.3 eV) for both samples. This can be explained that free carriers were generated under light, and the electrons were extracted by TiO₂ and transported to FTO, becoming more negative. The SPV of 1.0MABr sample is more negative than the control sample, indicating the more efficient electron extraction for the 1.0MABr sample.

Considering the fast hole transfer, we estimated the electron diffusion length through a diffusion model previously used for dye-sensitized solar cells,^[32] by assuming excited holes could be fast collected while the electron extraction is less efficient. Combining the optical absorption and device IPCE, the electron diffusion lengths for control film and 1.0MABr film were ≈ 65 and 105 nm, respectively (Figure S13, Supporting Information). Detailed analysis can be found in Supporting Information. The improved electron diffusion length agrees well with the result of reduced trap density and improved solar cell performance. However, the diffusion length is still quite lower than lead halide perovskites (over 2 μ m),^[33] which could be an essential cause of the low efficiency in double perovskite $Cs_2AgBiBr_6$ solar cell.

We therefore infer the mechanism of improved solar cell performance as Figure 4g,h. According to previous theoretical studies, abundant deep electron traps and shallow hole traps are easily formed within $Cs_2AgBiBr_6$, and the deep electron traps can impede charge carrier collection in solar cells.^[34] In our work, the intermediate Cs/MA mixed cation double perovskite assist the formation high quality double perovskite film, suppressing the defect formation. As a result of reduced electron traps and hole traps, photo-generated carriers can be extracted by both electrodes more efficiently, especially the enhancement in electron transfer process, contributing to the improved photocurrent and FF. We therefore infer that the abundant deep electron traps in double perovskite $Cs_2AgBiBr_6$ could be the main limitation for high-efficiency photovoltaic application.

2.6. Volatile Salts with Different Cations

Besides MABr, volatile bromide salts with two different cations, formamidineium bromide (FABr) and ammonium (NH₄Br) were further investigated as additives for $Cs_2AgBiBr_6$, using the

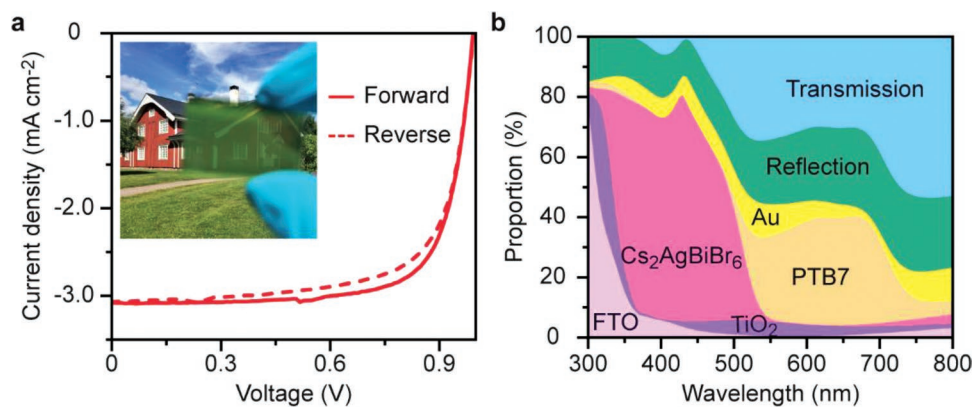


Figure 5. Semitransparent solar cell application. a) J - V curves under AM 1.5G illumination with both forward (dash line) and reverse (solid line) scan direction for the champion semitransparent device, with 10 nm of Au anode. b) Proportion spectra of the light absorption (by each layer of device), transmission and reflection.

similar fabrication process at the optimum ratio. Figure S15, Supporting Information, shows the surface SEM images of the annealed $\text{Cs}_2\text{AgBiBr}_6\text{-1.0FABr}$ and $\text{Cs}_2\text{AgBiBr}_6\text{-1.0NH}_4\text{Br}$. It is obvious that neither FABr nor NH_4Br additives can induce better crystallization for $\text{Cs}_2\text{AgBiBr}_6$ double perovskite films. The films fabricated from FABr and NH_4Br exhibited poorer surface coverage than MABr additive.

XRD experiments were also carried out on the initial films with different additives to study whether FA^+ and NH_4^+ can dope the $\text{Cs}_2\text{AgBiBr}_6$ double perovskite lattice, as shown in Figure S16, Supporting Information. Only the XRD peak of the $\text{Cs}_2\text{AgBiBr}_6\text{-1.0MABr}$ film was shifted left compared to those of the initial films, which confirms the formation of Cs/MA mixed double perovskite lattice. The films with FABr and NH_4Br additives did not show obvious shift at XRD peak. Considering the different cation radius (NH_4^+ 1.4 Å, Cs^+ 1.67 Å, MA^+ 1.8 Å, FA^+ 1.9–2.2 Å),^[35] we infer that halide salt additive with similar cation size as Cs^+ is the better choice for crystallization manipulation.

To analyze the effect of different additives on solar cell performances, both $\text{Cs}_2\text{AgBiBr}_6\text{-1.0FABr}$ and $\text{Cs}_2\text{AgBiBr}_6\text{-1.0NH}_4\text{Br}$ were employed into the optimized solar cell structure. The J - V characteristics of solar cells with different cation additives are compared in Figure S17, Supporting Information. The $\text{Cs}_2\text{AgBiBr}_6\text{-1.0FABr}$ and $\text{Cs}_2\text{AgBiBr}_6\text{-1.0NH}_4\text{Br}$ devices have shown slight improvement of PCE compared to control devices. The better surface morphology and dense film for device with MABr additive than those of the FABr and NH_4Br indicate that the unique effects of MABr additive for $\text{Cs}_2\text{AgBiBr}_6$ based double perovskite system. Therefore, the cation of the additive is important for the crystallization of the halide double perovskite system, because the similar cation size of MA^+ and Cs^+ to form Cs/MA cation mixed double perovskite intermediate phase.

2.7. Semitransparent Device Application

The high bandgap nature makes $\text{Cs}_2\text{AgBiBr}_6$ a suitable candidate for semitransparent photovoltaic application, which is appealing in wide areas, such as building integrated photovoltaics and windows. For evaluation the potential of $\text{Cs}_2\text{AgBiBr}_6$,

we employed the optimized $\text{Cs}_2\text{AgBiBr}_6\text{-1.0MABr}$ sample into a semitransparent structure, with same charge transport layers, but a thin Au layer (10 nm) as semitransparent anode. Inset of Figure 5a is the image of fabricated $\text{Cs}_2\text{AgBiBr}_6$ semitransparent device. PCE and average visible transmittance (AVT) are two critical parameters to depict the semitransparent devices. Figure 5a shows the J - V characteristics of the best-performed device under both forward and reverse scan direction, and the photovoltaic parameters are summarized in Table 3. Compared to the opaque $\text{Cs}_2\text{AgBiBr}_6$ solar cell (PCE = 2.53%), we observe slight performance loss and negligible hysteresis in the semitransparent device (PCE = 2.31%). Based on previous work, the calculation of AVT is expressed as:^[36]

$$AVT = \frac{\sum_{\lambda=380\text{nm}}^{780\text{nm}} T(\lambda) D_{\lambda} V(\lambda) \Delta\lambda}{\sum_{\lambda=380\text{nm}}^{780\text{nm}} D_{\lambda} V(\lambda) \Delta\lambda} \quad (5)$$

where $T(\lambda)$ is the wavelength-dependent transmittance spectra, which was measured for whole device; D_{λ} represents the relative spectral power distribution of standard illuminant D65, $\Delta\lambda$ is the wavelength interval, and $V(\lambda)$ represents the photopic response of the human eye. Our calculation was based on the spreadsheet calculator provided by Lunt's group,^[37] through inputting the transmittance data, then obtaining the AVT of 31.81%.

In an ideal semitransparent device, the illuminated light is aimed to be either absorbed by the active layer for current conversion, or transmitted through the device for higher transparency. Therefore, deep understanding of the optical distribution and loss is important for further optimization. Figure 5b presents the proportion spectrum of the incoming light within the semitransparent device. Most visible photons were absorbed by the photoactive layer or transmitted through

Table 3. The photovoltaic performance of the champion semitransparent solar cell device.

PSCs	V_{oc} [V]	J_{sc} [mA cm^{-2}]	FF	PCE [%]
Reverse	0.99	3.07	0.76	2.31
Forward	0.99	3.04	0.75	2.27

the whole device. Other layers, such as FTO, TiO₂, and thin Au anode still have a small portion of light absorption. However, the absorption by PTB7 and device reflection could account for the main optical losses. Further enhancement of Cs₂AgBiBr₆ semitransparent device performance is highly possible to be achieved through optical optimization of an antireflection layer and a suitable hole transport layer which has less photo-absorption while maintaining the efficient hole transport properties.

3. Conclusion

In summary, Cs₂AgBiBr₆ double perovskite with improved optoelectronic properties and suppressed trap formation was obtained by adding organic bromide additive with suitable cation (MA⁺) into precursor solution for crystallization regulation. According to our investigation, the introduced organic cation, MA⁺, can be doped into the cubic double perovskite lattice to form a Cs/MA mixed-cation double perovskite intermediate phase. The MA⁺ cation can help to form more ordered framework, and is thereafter evaporated under high temperature annealing. The obtained all-inorganic Cs₂AgBiBr₆ double perovskite exhibited improved film quality and emission intensity, as well as longer carrier lifetime due to the reduced trap density. With this strategy, the PCE for the best-performing solar cell reached 2.53%, increased from the control device with PCE of 1.43%, with negligible hysteresis. The increased PCE is mainly ascribed to the enhancement of *J*_{SC} and FF, as a result of the promoted electron collection between perovskite and TiO₂ layer. Furthermore, an efficient lead-free semitransparent photovoltaic application was demonstrated, with PCE of 2.31% and AVT of 31.81%, when employing the MABr-optimized Cs₂AgBiBr₆ double perovskite.

Supporting Information

Supporting Information is available from the Wiley Online Library or from the author.

Acknowledgements

The authors acknowledge the financial support obtained from the Swedish Research Council (V.R.), ÅForsk, Olle Engkvist Foundation and Swedish Energy Agency. X.Z. thanks the funding from the National Natural Science Foundation of China (51872014), the Recruitment Program of Global Experts, Fundamental Research Funds for the Central Universities, and the "111" project (B17002). The authors acknowledge Shengyang Zhou and Dr. Haoliang Cheng for great help during data analysis and preparation of nickel oxide thin-films.

Conflict of Interest

The authors declare no conflict of interest.

Data Availability Statement

The data that support the findings of this study are available from the corresponding author upon reasonable request.

Keywords

Cs₂AgBiBr₆, lead-free double perovskites, power conversion efficiency, solar cells, trap site density

Received: September 16, 2021

Revised: November 24, 2021

Published online: December 18, 2021

- [1] A. Kojima, K. Teshima, Y. Shirai, T. Miyasaka, *J. Am. Chem. Soc.* **2009**, *131*, 6050.
- [2] J. Jeong, M. Kim, J. Seo, H. Lu, P. Ahlawat, A. Mishra, Y. Yang, M. A. Hope, F. T. Eickemeyer, M. Kim, Y. J. Yoon, I. W. Choi, B. P. Darwich, S. J. Choi, Y. Jo, J. H. Lee, B. Walker, S. M. Zakeeruddin, L. Emsley, U. Rothlisberger, A. Hagfeldt, D. S. Kim, M. Grätzel, J. Y. Kim, *Nature* **2021**, *592*, 381.
- [3] Z.-K. Tan, R. S. Moghaddam, M. L. Lai, P. Docampo, R. Higler, F. Deschler, M. Price, A. Sadhanala, L. M. Pazos, D. Credgington, F. Hanusch, T. Bein, H. J. Snaith, R. H. Friend, *Nat. Nanotechnol.* **2014**, *9*, 687.
- [4] Y. Lee, J. Kwon, E. Hwang, C. H. Ra, W. J. Yoo, J. H. Ahn, J. H. Park, J. H. Cho, *Adv. Mater.* **2015**, *27*, 41.
- [5] M. A. Green, A. Ho-Baillie, H. J. Snaith, *Nat. Photonics* **2014**, *8*, 506.
- [6] a) T. Leijtens, G. E. Eperon, N. K. Noel, S. N. Habisreutinger, A. Petrozza, H. J. Snaith, *Adv. Energy Mater.* **2015**, *5*, 1500963; b) A. Babayigit, A. Ethirajan, M. Muller, B. Conings, *Nat. Mater.* **2016**, *15*, 247.
- [7] a) F. Giustino, H. J. Snaith, *ACS Energy Lett.* **2016**, *1*, 1233; b) G. Volonakis, A. A. Haghighirad, H. J. Snaith, F. Giustino, *J. Phys. Chem. Lett.* **2017**, *8*, 3917; c) X.-G. Zhao, J.-H. Yang, Y. Fu, D. Yang, Q. Xu, L. Yu, S.-H. Wei, L. Zhang, *J. Am. Chem. Soc.* **2017**, *139*, 2630; d) X.-G. Zhao, D. Yang, J.-C. Ren, Y. Sun, Z. Xiao, L. Zhang, *Joule* **2018**, *2*, 1662.
- [8] F. Igbari, Z. K. Wang, L. S. Liao, *Adv. Energy Mater.* **2019**, *9*, 1803150.
- [9] a) M. R. Filip, S. Hillman, A. A. Haghighirad, H. J. Snaith, F. Giustino, *J. Phys. Chem. Lett.* **2016**, *7*, 2579; b) E. T. McClure, M. R. Ball, W. Windl, P. M. Woodward, *Chem. Mater.* **2016**, *28*, 1348; c) A. H. Slavney, T. Hu, A. M. Lindenberg, H. I. Karunadasa, *J. Am. Chem. Soc.* **2016**, *138*, 2138; d) H.-J. Feng, W. Deng, K. Yang, J. Huang, X. C. Zeng, *J. Phys. Chem. C* **2017**, *121*, 4471.
- [10] R. L. Hoye, L. Eyre, F. Wei, F. Brivio, A. Sadhanala, S. Sun, W. Li, K. H. Zhang, J. L. MacManus-Driscoll, P. D. Bristowe, *Adv. Mater. Interfaces* **2018**, *5*, 1800464.
- [11] a) G. Volonakis, M. R. Filip, A. A. Haghighirad, N. Sakai, B. Wenger, H. J. Snaith, F. Giustino, *J. Phys. Chem. Lett.* **2016**, *7*, 1254; b) G. Longo, S. Mahesh, L. R. V. Buizza, A. D. Wright, A. J. Ramadan, M. Abdi-Jalebi, P. K. Nayak, L. M. Herz, H. J. Snaith, *ACS Energy Lett.* **2020**, *5*, 2200; c) W. Ning, F. Wang, B. Wu, J. Lu, Z. Yan, X. Liu, Y. Tao, J. M. Liu, W. Huang, M. Fahlman, *Adv. Mater.* **2018**, *30*, 1706246.
- [12] W. Pan, H. Wu, J. Luo, Z. Deng, C. Ge, C. Chen, X. Jiang, W.-J. Yin, G. Niu, L. Zhu, L. Yin, Y. Zhou, Q. Xie, X. Ke, M. Sui, J. Tang, *Nat. Photonics* **2017**, *11*, 726.
- [13] C. Wu, Q. Zhang, Y. Liu, W. Luo, X. Guo, Z. Huang, H. Ting, W. Sun, X. Zhong, S. Wei, *Adv. Sci.* **2018**, *5*, 1700759.
- [14] a) W. Gao, C. Ran, J. Xi, B. Jiao, W. Zhang, M. Wu, X. Hou, Z. Wu, *ChemPhysChem* **2018**, *19*, 1696; b) D. Zhao, B. Wang, C. Liang, T. Liu, Q. Wei, S. Wang, K. Wang, Z. Zhang, X. Li, S. Peng, G. Xing, *Sci. China Mater.* **2020**, *63*, 1518.
- [15] a) E. Greul, M. L. Petrus, A. Binek, P. Docampo, T. Bein, *J. Mater. Chem. A* **2017**, *5*, 19972; b) F. Igbari, R. Wang, Z. K. Wang, X. J. Ma, Q. Wang, K. L. Wang, Y. Zhang, L. S. Liao, Y. Yang, *Nano Lett.* **2019**, *19*, 2066.

- [16] Z. Zhang, C. Wu, D. Wang, G. Liu, Q. Zhang, W. Luo, X. Qi, X. Guo, Y. Zhang, Y. Lao, B. Qu, L. Xiao, Z. Chen, *Org. Electron.* **2019**, *74*, 204.
- [17] N. Pai, J. Lu, M. Wang, A. S. R. Chesman, A. Seeber, P. V. Cherepanov, D. C. Senevirathna, T. R. Gengenbach, N. V. Medhekar, P. C. Andrews, U. Bach, A. N. Simonov, *J. Mater. Chem. A* **2020**, *8*, 2008.
- [18] M. Pantaler, K. T. Cho, V. I. Queloz, I. s. García Benito, C. Fetzkenhauer, I. Anusca, M. K. Nazeeruddin, D. C. Lupascu, G. Grancini, *ACS Energy Lett.* **2018**, *3*, 1781.
- [19] J. Cho, J. T. DuBose, P. V. Kamat, *Chem. Mater.* **2019**, *32*, 510.
- [20] a) X. Yang, Y. Chen, P. Liu, H. Xiang, W. Wang, R. Ran, W. Zhou, Z. Shao, *Adv. Funct. Mater.* **2020**, *30*, 2001557; b) Z. Li, P. Wang, C. Ma, F. Igbari, Y. Kang, K.-L. Wang, W. Song, C. Dong, Y. Li, J. Yao, *J. Am. Chem. Soc.* **2021**, *143*, 2593; c) B. Wang, N. Li, L. Yang, C. Dall'Agnese, A. K. Jena, S.-i. Sasaki, T. Miyasaka, H. Tamiaki, X.-F. Wang, *J. Am. Chem. Soc.* **2021**, *143*, 2207.
- [21] H. Tan, F. Che, M. Wei, Y. Zhao, M. I. Saidaminov, P. Todorović, D. Broberg, G. Walters, F. Tan, T. Zhuang, *Nat. Commun.* **2018**, *9*, 1.
- [22] a) C. F. J. Lau, Z. Wang, N. Sakai, J. Zheng, C. H. Liao, M. Green, S. Huang, H. J. Snaith, A. Ho-Baillie, *Adv. Energy Mater.* **2019**, *9*, 1901685; b) J. Zhang, Z. Wang, A. Mishra, M. Yu, M. Shasti, W. Tress, D. J. Kubicki, C. E. Avalos, H. Lu, Y. Liu, *Joule* **2020**, *4*, 222; c) H. Wang, Z. Dong, H. Liu, W. Li, L. Zhu, H. Chen, *Adv. Energy Mater.* **2021**, *11*, 2002940.
- [23] a) F. Wei, Z. Deng, S. Sun, F. Zhang, D. M. Evans, G. Kieslich, S. Tominaka, M. A. Carpenter, J. Zhang, P. D. Bristowe, A. K. Cheetham, *Chem. Mater.* **2017**, *29*, 1089; b) R. Yin, G. Yu, W.-Y. Cong, C. Guan, J. Li, Y.-B. Lu, *ACS Appl. Mater. Interfaces* **2020**, *12*, 44798.
- [24] Z. Shao, Z. Wang, Z. Li, Y. Fan, H. Meng, R. Liu, Y. Wang, A. Hagfeldt, G. Cui, S. Pang, *Angew. Chem., Int. Ed.* **2019**, *58*, 5587.
- [25] D. T. Moore, H. Sai, K. W. Tan, D.-M. Smilgies, W. Zhang, H. J. Snaith, U. Wiesner, L. A. Estroff, *J. Am. Chem. Soc.* **2015**, *137*, 2350.
- [26] M. B. Johansson, B. Philippe, A. Banerjee, D. Phuyal, S. Mukherjee, S. Chakraborty, M. Cameau, H. Zhu, R. Ahuja, G. Boschloo, H. Rensmo, E. M. J. Johansson, *Inorg. Chem.* **2019**, *58*, 12040.
- [27] F. Zu, P. Amsalem, D. A. Egger, R. Wang, C. M. Wolff, H. Fang, M. A. Loi, D. Neher, L. Kronik, S. Duhm, N. Koch, *J. Phys. Chem. Lett.* **2019**, *10*, 601.
- [28] B. J. Kim, G. Boschloo, *Nanoscale* **2021**, *13*, 11478.
- [29] a) Q. Chen, H. Zhou, T.-B. Song, S. Luo, Z. Hong, H.-S. Duan, L. Dou, Y. Liu, Y. Yang, *Nano Lett.* **2014**, *14*, 4158; b) D.-Y. Son, J.-W. Lee, Y. J. Choi, I.-H. Jang, S. Lee, P. J. Yoo, H. Shin, N. Ahn, M. Choi, D. Kim, N.-G. Park, *Nat. Energy* **2016**, *1*, 16081.
- [30] X. Zhang, P. K. Santra, L. Tian, M. B. Johansson, H. Rensmo, E. M. J. Johansson, *ACS Nano* **2017**, *11*, 8478.
- [31] a) Z. Zhu, J. Ma, Z. Wang, C. Mu, Z. Fan, L. Du, Y. Bai, L. Fan, H. Yan, D. L. Phillips, S. Yang, *J. Am. Chem. Soc.* **2014**, *136*, 3760; b) H. Li, W. Shi, W. Huang, E.-P. Yao, J. Han, Z. Chen, S. Liu, Y. Shen, M. Wang, Y. Yang, *Nano Lett.* **2017**, *17*, 2328.
- [32] S. Soedergren, A. Hagfeldt, J. Olsson, S.-E. Lindquist, *J. Phys. Chem.* **1994**, *98*, 5552.
- [33] B. Chen, S.-W. Baek, Y. Hou, E. Aydin, M. De Bastiani, B. Scheffel, A. Proppe, Z. Huang, M. Wei, Y.-K. Wang, E.-H. Jung, T. G. Allen, E. Van Kerschaver, F. P. García de Arquer, M. I. Saidaminov, S. Hoogland, S. De Wolf, E. H. Sargent, *Nat. Commun.* **2020**, *11*, 1257.
- [34] a) Z. Xiao, W. Meng, J. Wang, Y. Yan, *ChemSusChem* **2016**, *9*, 2628; b) T. Li, X. Zhao, D. Yang, M.-H. Du, L. Zhang, *Phys. Rev. Appl.* **2018**, *10*, 041001.
- [35] R. D. Shannon, *Acta Crystallogr., Sect. A: Found. Adv.* **1976**, *A32*, 751.
- [36] G. Liu, C. Wu, Z. Zhang, Z. Chen, L. Xiao, B. Qu, *Sol. RRL* **2020**, *4*, 2000056.
- [37] C. Yang, D. Liu, M. Bates, M. C. Barr, R. R. Lunt, *Joule* **2019**, *3*, 1803.